AGU PUBLICATIONS

JGR

Journal of Geophysical Research: Atmospheres

RESEARCH ARTICLE

10.1002/2014JD021663

Key Points:
- Infrasonic interferometry can be applied to microbaroms
- The infrasonic wave of microbaroms is coherent up to a distance of 40 km
- The estimation of surface wind speed by infrasonic interferometry is possible

Supporting Information:
- Readme
- Figure S1
- Figure S2

Correspondence to:
J. T. Fricke,
fricke@knmi.nl

Citation:
Fricke, J. T., L. G. Evers, P. S. M. Smets, K. Wapenaar, and D. G. Simons (2014), Infrasonic interferometry applied to microbaroms observed at the Large Aperture Infrasound Array in the Netherlands, *J. Geophys. Res. Atmos.*, *119*,9654–9665, doi:10.1002/2014JD021663.

Received 19 FEB 2014
Accepted 29 JUL 2014
Accepted article online 4 AUG 2014
Published online 19 AUG 2014

Infrasonic interferometry applied to microbaroms observed at the Large Aperture Infrasound Array in the Netherlands

J. T. Fricke[1,2,3], L. G. Evers[1,2], P. S. M. Smets[1,2], K. Wapenaar[2], and D. G. Simons[3]

[1]Seismology Division, Royal Netherlands Meteorological Institute, De Bilt, Netherlands, [2]Department of Geoscience and Engineering, Faculty of Civil Engineering and Geosciences, Delft University of Technology, Delft, Netherlands, [3]Acoustic Remote Sensing Group, Faculty of Aerospace Engineering, Delft University of Technology, Delft, Netherlands

Abstract We present the results of infrasonic interferometry applied to microbaroms, obtained from ambient noise. For this purpose the "Large Aperture Infrasound Array" (LAIA) was used, which has been installed in the Netherlands. Preprocessing appeared to be an essential step in enhancing the microbarom signals from ambient noise that strongly influences the results of the interferometry. Both the state of the atmosphere and the noise characteristics are taken into account to assess the strength of the cross correlation. The delay time of the microbaroms between two stations is determined through cross correlating the recordings. By calculating the cross correlations between all 55 station pairs of LAIA, we are able to find the delay time of microbaroms up to a interstation distance of 40.6 km. Using the strength of the cross correlations, we are able to show that the coherence of the microbaroms along the direction of arrival is higher than orthogonal to it. A comparison of the atmospheric state, with a cross correlation, over a period of 10 days, reveals that the infrasound propagation over the array is correlated with the tropospheric temperature and wind. Based on the cross correlations between the three closest stations, we are able to passively estimate the effective sound speed and the wind speed as a function of time.

1. Introduction

It has recently been shown that the variability of the (upper) atmosphere can be probed using infrasound. *Le Pichon et al.* [2005] and *Antier et al.* [2007] demonstrated that continuous infrasound monitoring of volcanoes provides means for probing fine-scale wind fluctuations from the ground to the stratosphere. *Lalande et al.* [2012] developed an inverse model to investigate the capability of infrasound observations as a remote sensing technique. Observing the Tungurahua volcano in Ecuador, *Assink et al.* [2012, 2013] showed that infrasonic remote sensing of wind can be applied to the upper atmosphere. Even the effects of small-scale atmospheric gravity wave fluctuations can be found in infrasound measurements as shown by *Drob et al.* [2013]. For the troposphere, *Marcillo and Johnson* [2010] demonstrated that the wind vector can be obtained with three infrasound sensors in the near field of a volcano.

In general, such studies depend on ground truth events, i.e., an explosion or a volcanic eruption. This is a disadvantage because the exact time and location of these events are need to be known. Furthermore, there is only a limited occurrence of such ground truth events.

Ambient infrasonic noise consists mostly of microbaroms [*Posmentier*, 1967]. These microbaroms result from the nonlinear interaction of oceanic waves and are almost continuously present at a frequency of 0.2 Hz [*Brekhovskikh et al.*, 1973; *Donn and Naini*, 1973]. Atmospheric temperature and wind can be retrieved from microbaroms using infrasonic interferometry, which is based on the theory of nonreciprocal Green's function retrieval by cross correlation [*Wapenaar*, 2006; *Godin*, 2006]. This theory determines the outcome of the cross correlation of the measured noise field at two receivers A and B in a moving medium. Assuming that the noise field is equipartitioned, this cross correlation converges to the Green's function from receiver A to receiver B plus the time-reversed Green's function from receiver B to receiver A, convolved with the autocorrelation of the noise. In other words, the delay times between the two receivers in both directions can be determined by cross correlating the ambient noise at these two receivers. In a study with direct tropospheric waves measured at two locations, *Haney* [2009] has shown that interferometry can be applied to infrasonic ambient noise to retrieve temperature and the strength of winds in the troposphere.

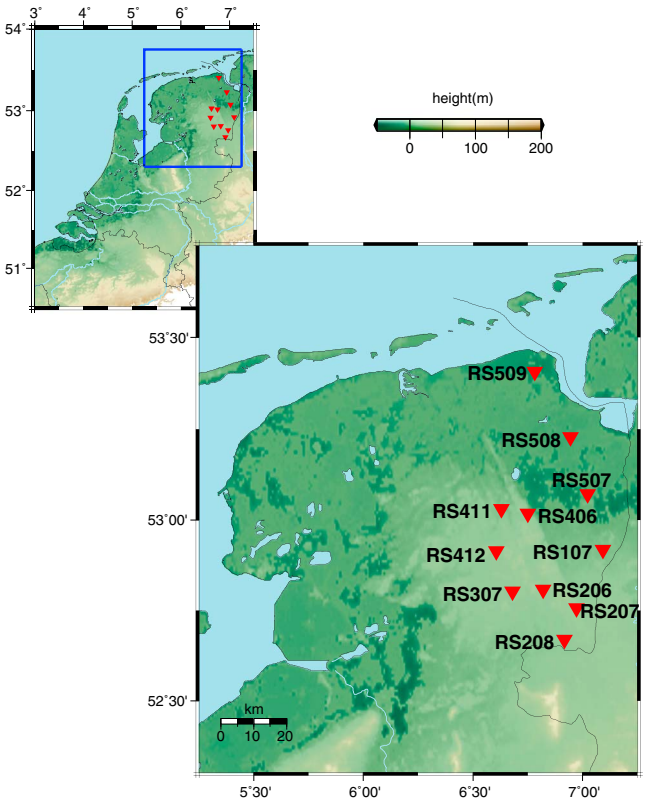

Figure 1. The Large Aperture Infrasound Array (LAIA) in the north of the Netherlands (52.91°N 6.87°E) consists of 11 microbarometers and has an aperture of 82.6 km.

In our recent paper [*Fricke et al.*, 2013], we applied infrasonic interferometry to synthetically generated microbaroms, which were refracted by the stratosphere to gather insight and prove their feasibility for probing the stratosphere. In a recent approach, *Godin et al.* [2014] were able to use traffic noise to estimate the wind vector in the troposphere, showing that the atmosphere can also be probed by ambient noise. Another technique using sound to probe the atmosphere is sonic detection and ranging. Such an active technique can be used to obtain wind and temperature of the lower atmosphere [*Crescenti*, 1997].

In this paper, we apply infrasonic interferometry to measured microbaroms. We investigate the distance up to which the infrasonic wave of the microbaroms is coherent by calculating the cross correlations between all 55 station pairs of the so-called "Large Aperture Infrasound Array" (LAIA) in the Netherlands. LAIA was installed at the site of the radioastronomical "Low-Frequency Array" [*van Haarlem et al.*, 2013]. The derived delay times are used to estimate the direction of arrival (DOA). Curve fitting of the coherence then gives the sound speed scatter and the scatter of the incident angle. Further, we compare the atmospheric state with the cross correlation over a period of 10 days. Based on the cross correlations between the three closest stations, we estimate the effective sound speed and the wind speed as a function of time.

The structure of this paper is as follows. Section 2 begins with a description of the "Large Aperture Infrasound Array" (LAIA) used to measure the ambient noise. Then, section 3 gives an overview of the processing of the ambient noise in order to extract microbaroms and discusses which processing steps are applied to the results of the cross correlations. In section 4, we discuss the atmospheric conditions during the time of interest and how microbaroms are generated. In section 5 we investigate the result of the cross correlations as a function of interstation distance and time. The first part of this section examines the coherence, while the latter compares the cross correlation results with the atmospheric variability. The last part enlists the conclusions from this study.

2. The Large Aperture Infrasound Array

In the north of the Netherlands the Royal Netherlands Meteorological Institute (KNMI) installed the "Large Aperture Infrasound Array" (LAIA), which consists of 11 infrasound receivers (microbarometers) and has an aperture of 82.6 km with its center at 52.91°N and 6.87°E (cf. Figure 1). The array can be characterized through a plot of the interstation distance versus the interstation orientation (cf. Figure 2). The orientation of the station combination is expressed as an azimuth angle. An angle of 0° (or 180°) indicates a north–south orientation and 90° (or 270°) an east-west orientation. Each station pair is orientated in two opposite directions. To avoid redundancy, Figure 2 presents only the angles from 0° to 180°. According to Figure 2 the interstation distances and orientations are well distributed, which avoids spatial aliasing [*Haubrich*, 1968].

The in-house developed microbarometers are able to measure infrasound up to a period of 1000 s with a sensitivity from 1 mPa up to tens of pascals. The period of 1000 s lies in the acoustic-gravity wave regime

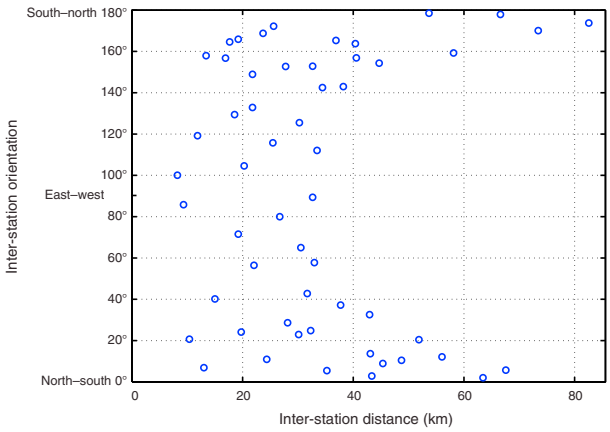

Figure 2. The interstation distance versus the interstation orientation of all possible station combinations of the Large Aperture Infrasound Array (LAIA). An angle of 0° indicates a north-south orientation and 90° an east-west orientation.

[*Mentink and Evers*, 2011]. The analog signal is digitized by a 24 bit A/D converter with a sample rate of 40 Hz. Each microbarometer is equipped with six porous hoses in a star-like configuration with a diameter of 10 m. This layout realizes analog noise reduction by spatial sampling. Because noise is mostly caused by wind, which has a small coherence length, it cancels out over the area of the spatial sampling. The signal of interest, i.e., the infrasonic wave, has a much larger wavelength and is not affected by the noise reducer.

3. Processing of Microbaroms and Cross Correlations

The microbaroms occur around 0.2 Hz and have amplitudes at the receiver of order of 0.1 Pa. Amplitudes of transients are often larger; for instance, sonic booms in the far field have amplitudes of up to 10 Pa. There are several methods known from seismic interferometry to suppress such disturbances [*Bensen et al.*, 2007]. In this section, we describe how we tailored these methods to infrasonic interferometry.

In the first processing step, the raw data are band-pass filtered in order to remove pressure fluctuations caused by wind and sources with frequencies outside of the microbarom band. Figure 3 shows an unfiltered (Figure 3a) and a band-pass filtered (Figure 3b) spectrogram of a recording. We used a second-order Butterworth band-pass filter with corner frequencies from 0.05 to 0.3 Hz. The peak around 0.2 Hz is caused by microbaroms. Figure 4a shows the cross correlations of band-pass filtered data recorded at stations RS206 and RS412 over 10 days. We chose these two stations since they lie along the expected direction of arrival (DOA) [*Evers and Haak*, 2001; *Kedar et al.*, 2008]. The data were split into moving time windows of 3 h, which had an overlap of 98% (≈ 2:56 h) to enhance the resolution. Figure 4a shows a distinct change in character

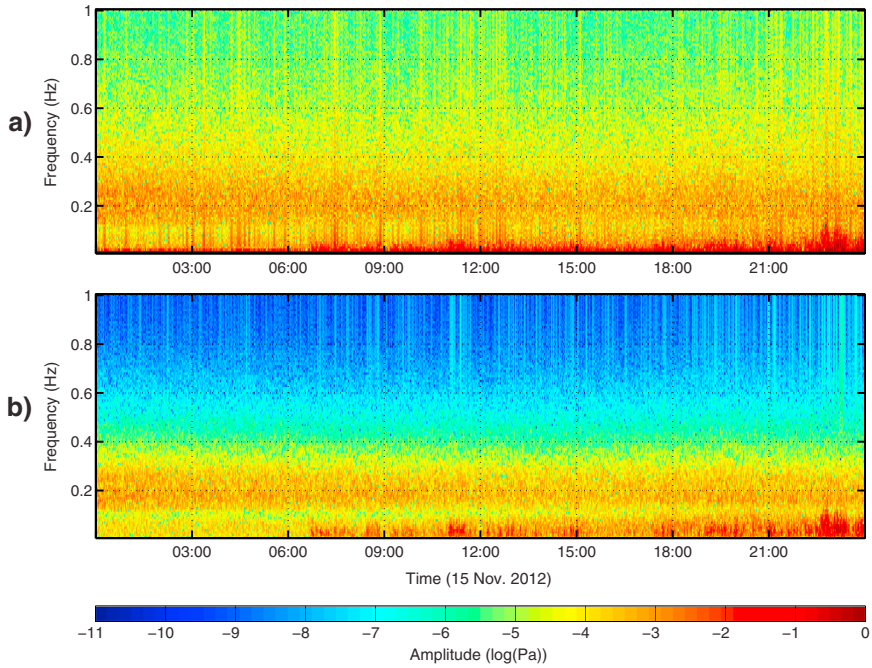

Figure 3. Spectrogram of a (a) recording unfiltered and (b) band-pass filtered. The peak around 0.2 Hz is caused by microbaroms.

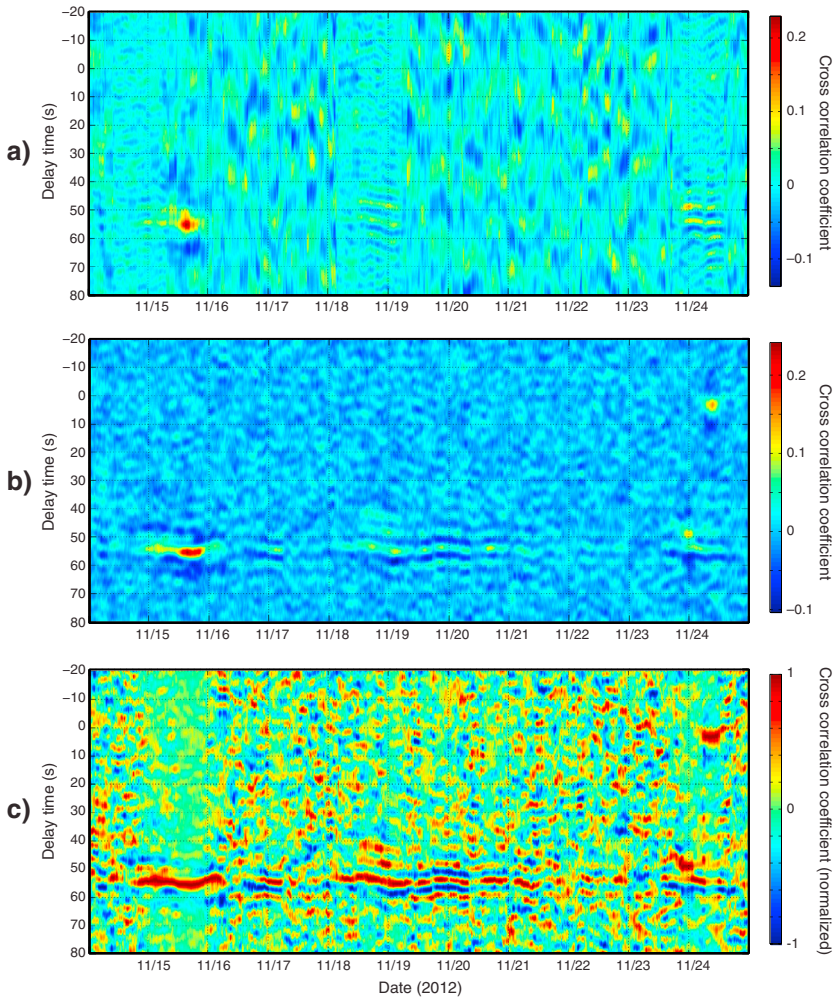

Figure 4. (a) The cross correlations of band-pass filtered data of 10 days, split into 3 h windows. The microbaroms can be found as a peak (red spot) on 15 November 2012. The data were recorded at the stations RS206 and RS412 of LAIA. (b) The cross correlation of fully processed data after band-pass, temporal, and spectral normalization. (c) Normalized result of the cross correlation.

between 18 November 2012 and 19 November 2012 as well as just after 24 November 2012. These are periods in time, when there is less wind noise. In Figure 4a the microbaroms can be found as a strong peak (red spot) in the cross correlation on 15 November 2012 around 18:00 h, at a delay time of around 55 s.

The determined delay time of 55 s is reasonable for a direct path of 18.5 km, which is the distance between the recording stations RS206 and RS412. We used this known microbarom peak as a reference for determining the processing parameters in a trial and error approach. The performance of the parameters is determined by the sharpness of the peak, which can be measured by the signal-to-noise ratio (SNR). All processing steps were applied to the raw data before cross correlation in order to maximize the quality of the microbarom peak obtained after cross correlation.

Using this approach, we found the mentioned corner frequencies (0.05 Hz and 0.3 Hz) of the band pass. Next, we determined the settings for temporal normalization and spectral normalization (i.e., whitening) by trial and error. The temporal normalization raises weak signals of microbarom sources and reduces strong signals of transients like wind and blasts. It calculates the root-mean-square (RMS) of the data in a time window of a certain length and divides the sample in the center of the window by the obtained RMS. By trial and error, we found an optimal window length of 46 s. The spectral normalization flattens the spectrum of the recording. This also amplifies microbaroms by raising weak frequencies, whereas strong monochromatic disturbances are suppressed. We found a whitening band from 0.03 Hz to 0.21 Hz and a cosine taper

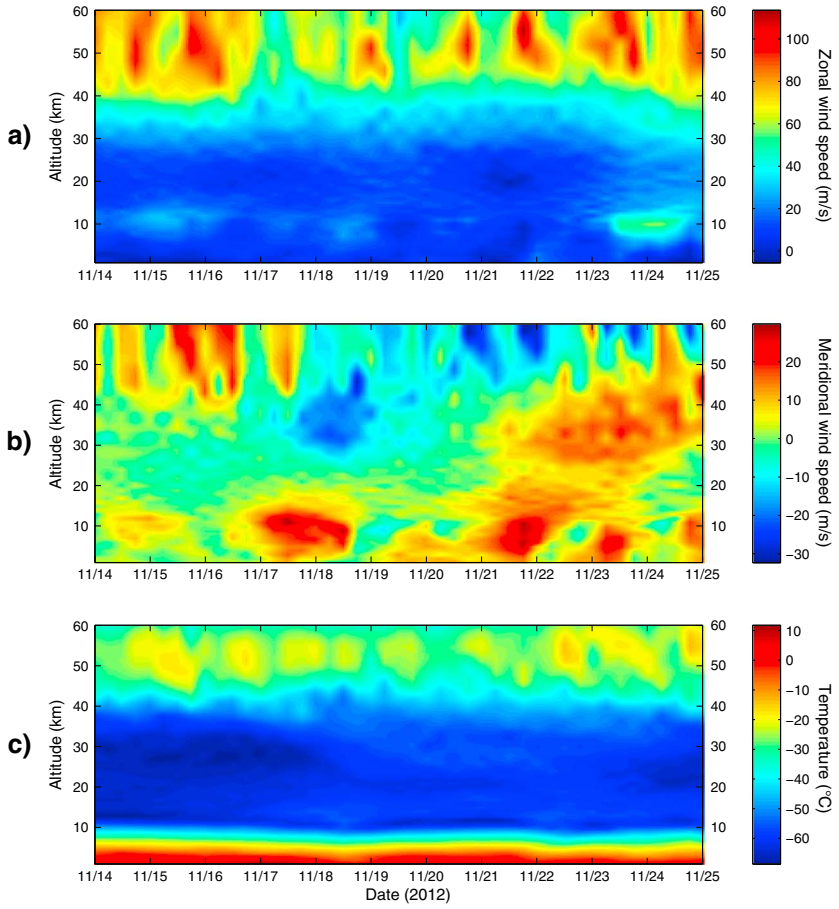

Figure 5. The atmospheric specifications (4 times per day) of the European Centre for Medium-Range Weather Forecasts (ECMWF) operational analysis high-resolution (HRES) model. This includes (a) the zonal wind, (b) the meridional wind, and (c) the temperature above the array (52.8°N/6.7°E grid nodes ECMWF).

applied to the ends of the spectra to result in the highest SNR. The cosine taper gives a smooth transition between these corner frequencies and the cutoff frequencies (0 Hz and 0.34 Hz). Figure 4b shows the cross correlations of the fully processed recordings of RS206 with RS412, using the parameters listed above for the band-pass, temporal, and spectral normalization. The normalized result of the cross correlation (Figure 4c) emphasizes the development of the delay time over several days.

4. State of the Atmosphere and Microbarom Sources

In the previous section we described how we found microbaroms for the period between 14 November and 24 November 2012. In this section we describe the influence of atmospheric conditions on the infrasound propagation during these 10 days and how we model the microbarom sources in simulations.

4.1. Atmospheric Conditions

Figure 5 shows the atmospheric specifications (4 times per day) of the operational analysis high-resolution model (ECMWF HRES) provided by the European Centre for Medium-Range Weather Forecasts. This includes the zonal wind, the meridional wind, and the temperature above the array (52.8°N, 6.7°E, grid node).

Gossard and Hooke [1975] described the influence of the atmospheric conditions on the infrasound propagation with the following equation:

$$c_{\mathrm{ef}}(z) = \sqrt{\gamma_g RT(z)} + \hat{n}_{\mathrm{DOA}} \cdot \vec{u}(z) \tag{1}$$

where $c_{\mathrm{ef}}(z)$ is the effective sound speed dependent on the altitude z, γ_g is the ratio of specific heats, R is the gas constant, $T(z)$ is the temperature in Kelvin, $\hat{n}_{\mathrm{DOA}}$ is the direction of the sound propagation, and $\vec{u}(z)$ is the wind vector. The first term of this equation describes the influence of the adiabatic sound speed

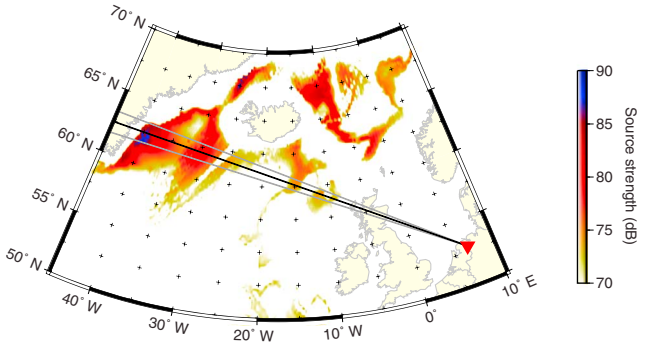

Figure 6. A map of the microbarom activity on 15 November 2012. Color coded is the microbarom source intensity for 0.05 Hz to 0.34 Hz, applying the *Waxler and Gilbert* [2006] model including bathymetry [*Waxler et al.*, 2007]. Ocean and weather data are obtained from the European Centre for Medium-Range Weather Forecasts (ECMWF). The black line shows the direction of arrival (DOA) for microbaroms of 310° and is calculated in a least squares estimation. The gray lines illustrate the angular scatter of ±1.3° (see section 5.1).

$(c_T(z) = \sqrt{\gamma_g RT(z)})$ and can be calculated using $\gamma_g R = 402.8\ \mathrm{m^2\ s^{-2}\ K^{-1}}$. The second term describes the influence of the wind on the effective sound speed and is a projection of the wind in the direction of the sound propagation. We describe in section 5.1 how the direction of arrival (DOA) is determined.

For the 10 days shown, there is a strong zonal wind in the stratosphere. This zonal wind is caused by the circumpolar vortex, which is directed eastward in a regular Northern Hemisphere winter. Sudden stratospheric warmings can change the direction and strength of the polar vortex [*Rind and Donn*, 1978; *Evers and Siegmund*, 2009]. At 10 km altitude we find the jet stream, which is more variable due to Rossby wave activity [*Holton*, 2004]. The increase in temperature in the stratosphere is caused by the ozone layer, which absorbs solar radiation. This increase will lead to an increase in $c_{\mathrm{ef}}(z)$ (see equation (1)), enabling the ducting of infrasound between the Earth's surface and the stratopause. In general, the zonal wind is stronger than the meridional wind.

4.2. Microbarom Sources

Large energetic systems of ocean waves, e.g., marine storms, hurricanes, and high-amplitude long-period ocean swell, radiate acoustic energy almost continually into both the ocean and the atmosphere [*Longuet-Higgins*, 1950; *Brekhovskikh et al.*, 1973]. The ocean component can couple to the ocean floor, radiating seismic energy into the solid Earth [*Gutenberg*, 1939; *Donn and Naini*, 1973]. The atmospheric component is referred to as microbaroms, whereas the seismic component is known as microseisms. Ocean surface wave interaction can cause second-order pressure oscillations, generating almost continuously coherent ambient noise at twice the ocean surface wave frequency [*Longuet-Higgins*, 1950; *Hasselmann*, 1963]. Microbarom signals are well characterized by a radiation frequency of 0.2 ± 0.1 Hz. Microbarom radiation can be fully modeled a two-fluid model, over air and seawater, and a sea-state model [*Waxler and Gilbert*, 2006]. Column resonance is allowed assuming an elastic seafloor, taken into account the bathymetry [*Waxler et al.*, 2007]. The *Waxler and Gilbert* [2006] source model is validated by *Walker* [2012] and *Stopa et al.* [2012], studying ambient swell and hurricane-induced microbaroms, respectively. The ECMWF high-resolution Wave Atmosphere Model (WAM) is used as sea-state model for microbarom modeling (model cycle 38r1, June 2012). The WAM model is coupled to the ECMWF HRES model, important for microbarom simulations. It is an analysis model, consisting of both model data and assimilated buoy and satellite data. The sea state is described by the 2-D wave spectra (2DFD), consisting of 36 frequencies and directions. Integration of the wave spectrum over direction and frequency results in the significant wave height for each longitude and latitude. Wave periods range from approximately 30 s down to 1 s, logarithmically spaced ($T_0/T_n = 1.1^{n-1}$), with a horizontal resolution of 0.25°. Model runs are available every 6 h, globally, with latitudes up to 85°. Applying the *Waxler and Gilbert* [2006] microbarom source model with bathymetry on ECMWF ocean wave spectra results in an energetic microbarom source region located around Iceland for the entire 10 day period. A map of the microbarom activity on 15 November 2012 is shown in Figure 6.

5. Retrieving Parameters of Infrasound Propagation and the Atmosphere

5.1. Cross Correlation and Coherence as a Function of Distance

After the optimization of the processing parameters, we determined the direction of arrival (DOA) and the maximum interstation distance for which the delay time can still be obtained by cross correlation. For this purpose, we calculated the cross correlations between all 55 possible station pairs of LAIA.

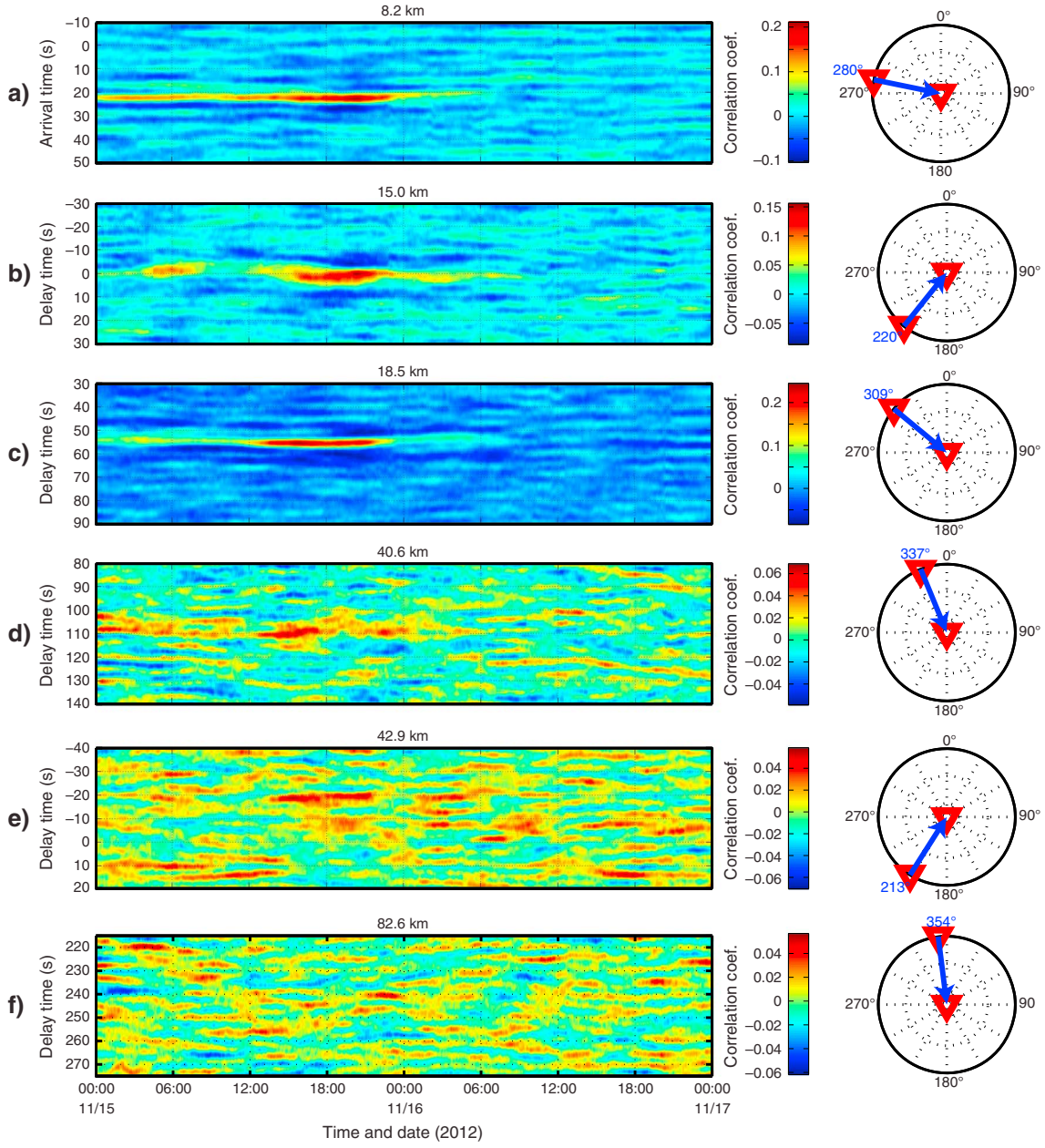

Figure 7. (a–f) The left-hand side shows the cross correlations of six selected station pairs in order of increasing distance. On the right the orientation of the pair is shown (0° is north, and 90° is east). The cross correlation of the smallest interstation distance (8.2 km, stations RS406–RS411) is shown in Figure 7a. The strongest cross correlation between RS206 and RS412 is shown in Figure 7c. 40.6 km is the maximal distance at which we still obtain a clear peak in the cross correlation (RS507–RS509) is shown in Figure 7d. The cross correlation of the largest interstation distance (82.6 km, RS208–RS509) is shown in Figure 7f.

The left column of Figure 7 shows the cross correlations of six selected station pairs in order of increasing distance. On the right, the orientation of the pair is shown (0° is north, and 90° is east). For distances over 40.6 km it becomes more difficult to identify the delay time in the cross correlation, since there are several peaks. All 39 cross correlations over smaller distances provide microbarom delay times (cf. Figure S2 in the supporting information).

Under the plane wave assumption, we are able to calculate the direction of arrival (DOA) in a least squares estimation using the 39 obtained delay times. Figure 6 shows the estimated DOA of 310° for the microbarom peak on 15 November 2012. It points to the northern Atlantic Ocean, a known source of microbaroms [*Evers and Haak*, 2001; *Kedar et al.*, 2008]. This direction also corresponds to region of microbarom sources found in the simulations of the microbarom source model (cf. section 4.2) indicated by the colors in Figure 6.

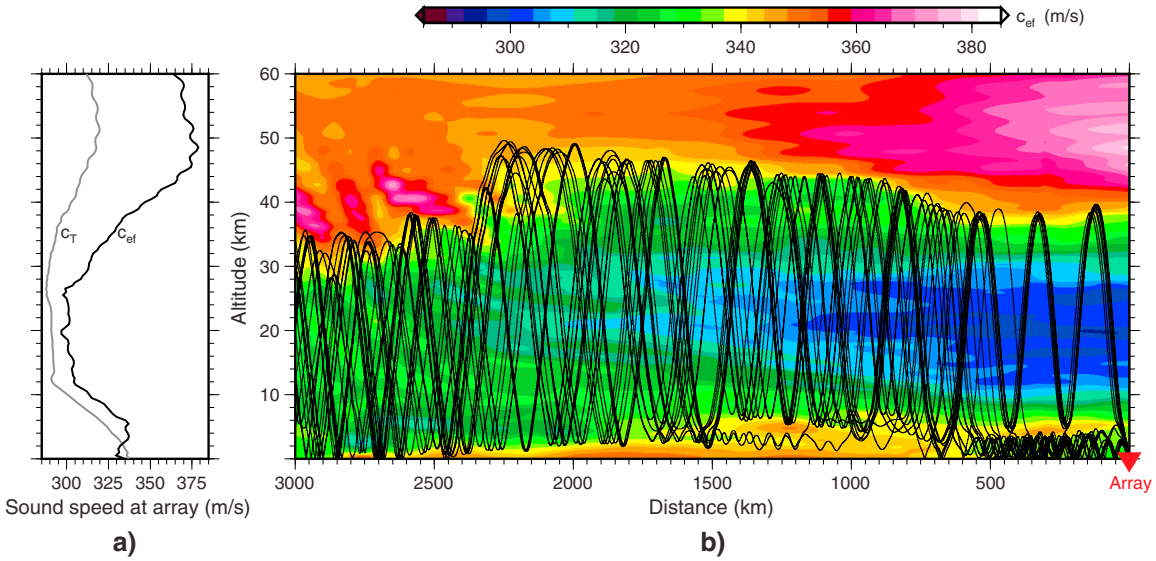

Figure 8. (a) Speed of sound $c_T(z)$ and effective sound speed $c_{ef}(z)$ at the center of LAIA (52.91°N 6.87°E). (b) The atmospheric trajectories generated by a ray tracer for a back azimuth of 310°. The ray tracing model takes temperature and wind profiles of 15 November 2012 into account. Temperature and wind profiles are calculated in a three-dimensional interpolation from data provided by ECMWF (see section 4). The paths indicate that the receivers of LAIA were reached by microbaroms which were first refracted in the stratosphere and then propagated tropospherically.

On 15 November this direction dominates the results of the cross correlations and the contribution of sources from other direction is negligible. The strongest cross correlation is achieved between RS206 and RS412 (Figure 7c) at 18.5 km. It is remarkable that the cross correlation at 18.5 km is stronger than all cross correlations of smaller distances (see Figures 7a and 7b). By examining the direction, we find that the orientation of RS206–RS412 is closest to the DOA. As an additional verification of the DOA, we modeled the microbarom propagation with a ray tracer. The ray tracing model takes temperature and wind profiles of 15 November into account. These profiles are calculated in a three-dimensional interpolation from data provided by ECMWF (see section 4). Figure 8 shows the simulated raypaths along the back azimuth plane of 310° obtained by a backward simulation from the array to the microbarom sources. The paths indicate that the receivers of LAIA were reached by microbaroms which were first refracted in the stratosphere and then propagated in the troposphere. The tropospheric rays in this figure have elevation angles between 0° and 9° from the horizontal.

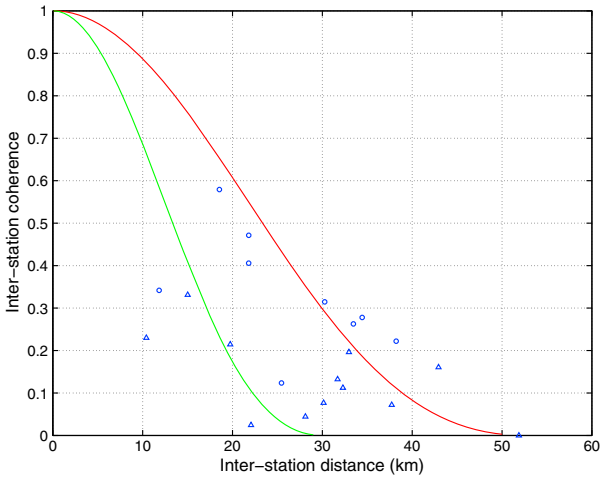

Figure 9. The interstation coherence sorted into two groups dependent on the direction of the station pair. In group A (dots) are all station pairs which are oriented parallel to the direction of arrival within ±22° (288°–332°). Group B (triangles) contains all station pairs which are oriented orthogonal to the direction of arrival within ±22° (198°–242°). The red curve is valid for sound speed scatter of $\Delta c = \pm 5.9$ m/s and the green curve for a angular scatter of $\theta = \pm 1.7°$.

Next, we study the influence of the station orientation on the coherence. Figure 9 shows the magnitude square coherence calculated for the station pairs on 15 November 2012, for the 3 h window from 14:52 h till 17:52. We chose this time window, because it contains the strongest peak (see Figure 4). The coherence (msc_{xy}) was calculated using a Hanning smoothing window of 18 min and the following equation [*Mack and Flinn*, 1971]:

$$msc^2_{xy}(f) = \frac{|G_{xy}(f)|^2}{G_x(f)G_y(f)}, \qquad (2)$$

where $G_x(f)$ and $G_y(f)$ are the autopower spectra and $G_{xy}(f)$ is the cross-power spectrum of the station pair. The recordings of

the stations were band-pass filtered (0.05 Hz–0.21 Hz) and temporal normalized (window length of 2.43 s) before the spectra were calculated (see section 3). Figure 9 shows the coherence of a spectral peak at 0.19 Hz. We split the coherencies into two groups according to the direction of the station pair. Group A (dots) consists of all station pairs which are oriented parallel to the DOA within ±22° (288°–332°), while to group B (triangles) belong all station pairs which are oriented orthogonal to the DOA within ±22° (198°–242°). All other pairs were disregarded. Figure 9 shows that the strength of the coherencies in group B diminishes more rapidly with increasing distance than in group A. *Mack and Flinn* [1971] have described this relation between distance, direction, and spatial coherence for acoustic-gravity waves with a period between 10 s and 100 s (equation (3)). According to *Mack and Flinn* [1971], the loss of coherence along the DOA (red curve in Figure 9) results from scattering and mode superposition, and the loss of coherence orthogonal to the DOA (green curve) is an effect of scattered waves which reach the stations from a range of azimuths:

$$\varepsilon^2(\vec{r}, f) = \left| \frac{\sin(2\pi k_0 x \sin\theta)}{2\pi k_0 x \sin\theta} \right|^2 \left| \frac{\sin(2\pi \Delta k y)}{2\pi \Delta k y} \right|^2, \tag{3}$$

where ε is a measure of the spatial coherence, f is the frequency, and $\vec{r}$ is the distance vector between the stations, which consists of the components x (orthogonal to DOA) and y (parallel to DOA). We assume the wave number k_0 to be 0.497 km^{-1} (with the frequency f = 0.19 Hz and the effective sound speed c_{ef} = 342 m/s). The angular scatter is θ, and Δk is a measure of the sound speed scatter Δc $\left(k_0 \pm \Delta k = \frac{f}{c_{ef} \mp \Delta c}\right)$. The term to the right of the product in equation (3) describes the coherence of group A, since the distances in x direction of these station pairs are negligible ($x \approx 0$). The term to the left describes the spatial coherence of group B ($y \approx 0$). By varying the angular scatter θ and the sound speed scatter Δc, we can estimate the two curves in Figure 9. The red curve in Figure 9 is valid for sound speed scatter of $\Delta c = \pm 5.9$ m/s and the green curve for an angular scatter of $\theta = \pm 1.7°$. The angular scatter corresponds to the accuracy of the DOA estimation (see gray lines in Figure 6). The velocity scatter corresponds to the accuracy of the sound speed and the wind speed estimation in the next section.

5.2. Cross Correlation and Atmospheric Variability as a Function of Time

In this section, we investigate whether a relation between the result of the cross correlation (Figure 4) and the atmospheric conditions (Figure 5) can be found.

Overall, we observed a decrease of the cross correlation strength with a strong meridional wind in the lower atmosphere (<10 km). This can be explained by the higher noise levels.

Figure 10a shows the cross correlation of the station pair RS206 and RS412. This is the strongest cross correlation of all station combinations (see section 5.1). As a reference, the white curve shows the adiabatic sound speed $c_{T,0}$ close to the two stations, which is calculated using surface temperature T measured by the KNMI. To take the influence of the wind into account, we projected the wind speed $\vec{u}$ in the DOA $\hat{n}_{DOA}$ and added it to the adiabatic sound speed $c_{T,0}$ (see equation (1)). Figure 10b shows the wind speed with black dots for the ground level and gray dots for the stratosphere at 39 km. Our numerical experiments with the ray tracer described in section 5.1 (Figure 8) found this altitude to be dominant in the refraction of microbaroms, urging an investigation of the stratospheric layer at a height of 39 km for influence on the propagation over the array. The corresponding wind direction is shown in Figure 10c (0° is north; 90° is east). The stratospheric wind speed and direction are provided by the ECMWF (see section 4), and the tropospheric wind speed and direction are measured by the KNMI. In section 5.1 we obtained 310° as the DOA of the microbaroms (red line in Figure 10c), which is used for the projection of the wind.

We calculated the correlation coefficient between the result of the cross correlation and the different sound speeds (adiabatic surface sound speed $c_{T,0}$, effective surface sound speed $c_{ef,0}$, and effective stratospheric sound speed $c_{ef,39}$), in order to quantify their relation (cf. table 1). We found a higher correlation between tropospheric sound speeds ($c_{T,0}$, $c_{ef,0}$) and infrasonic delay time than between stratospheric sound speed ($c_{ef,39}$) and infrasonic delay time. This indicates that tropospheric wind and temperature have a stronger influence on the microbarom propagation over the array than stratospheric conditions; i.e., we observed tropospheric propagation near the stations. These results are corroborated by the ray tracing simulation (cf. section 5.1).

In the following section the influence of the tropospheric conditions on the delay time is studied further. For this purpose, we selected the cross correlations between the stations RS206, RS307, and RS412. Using these

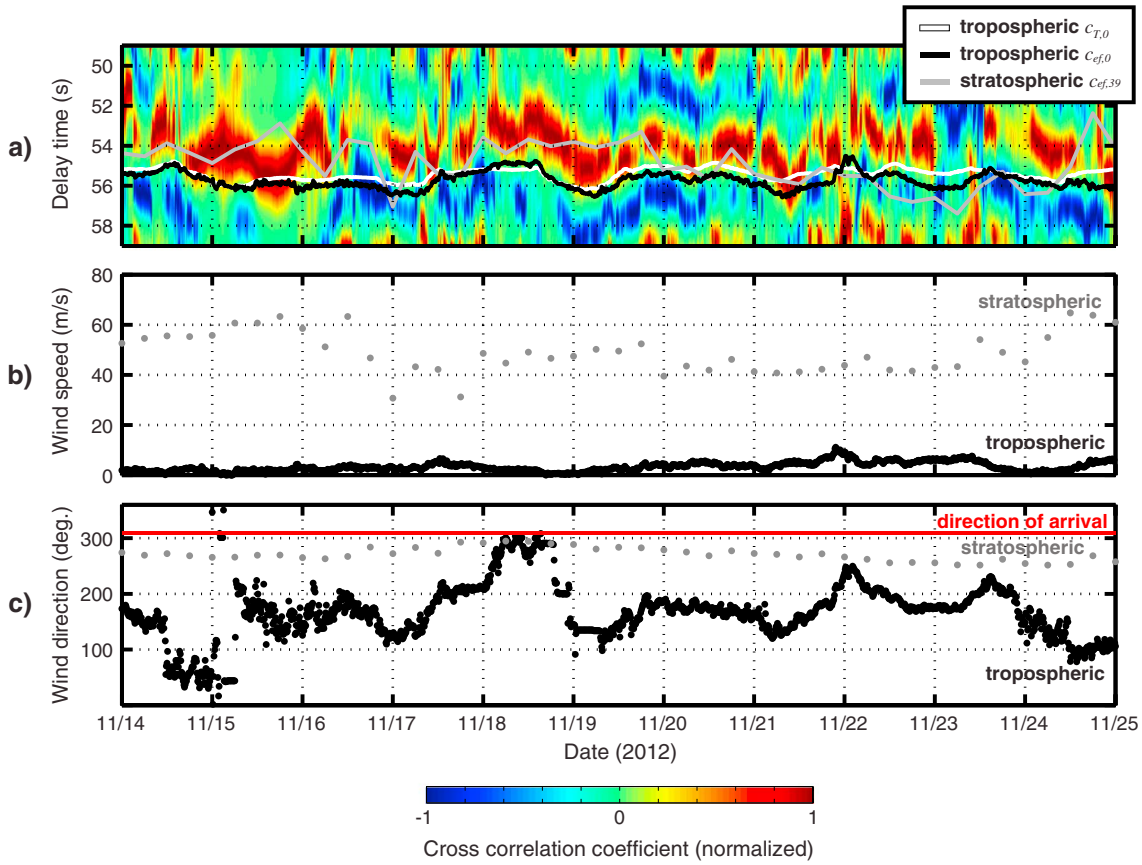

Figure 10. (a) Cross correlation of the station combination RS206 and RS412. The color indicates the normalized strength of the cross correlation. The white curve shows the arrival time of microbarom signals derived from adiabatic tropospheric sound speed $c_{T,0}$ at the two stations. The black curve indicates the arrival time derived from the effective tropospheric sound speed $c_{ef,0}$, and the gray curve the arrival time derived from the effective stratospheric sound speed $c_{ef,39}$. The tropospheric conditions were measured by the KNMI, and the stratospheric conditions were provided by ECMWF. (b) Wind speed in the troposphere (black dots) and in the stratosphere (gray dots). (c) Wind direction in the troposphere (black dots) and in the stratosphere (gray dots). The red line indicates the direction of arrival DOA.

values and the least squares estimation introduced in section 5.1, we estimated the effective surface sound speed $c_{est,0}$ over the three stations and the DOA for the whole period of 10 days. Figure 11a shows $c_{est,0}$ as red dots and $c_{ef,0}$ as a black line. We can see that the difference between $c_{ef,0}$ and $c_{est,0}$ was larger (10 m/s) in the first 2 days and became smaller (5 m/s) after 16 November. After 19 November the $c_{est,0}$ comes even closer to $c_{ef,0}$ (2 m/s).

Since $c_{est,0}$ consists of $c_{T,0}$ and the projected wind $\vec{u}$, we are able to estimate the wind speed between the three stations by subtracting $c_{T,0}$ from $c_{est,0}$. Figure 11b shows the estimated wind speed (red dots) and the wind speed (black line) provided by ECMWF. The difference between estimated wind and measured wind shows a similar trend to the sound speed estimation. The largest difference occurs during the first 2 days (10 m/s) and becomes smaller with around 5 m/s on 18 November till around 2 m/s after 19 November.

Table 1. Correlation Coefficients Between the Result of the Cross Correlation and the Different Sound Speeds (Adiabatic Surface Sound Speed $c_{T,0}$, Effective Surface Sound Speed $c_{ef,0}$, and Effective Stratospheric Sound Speed $c_{ef,39}$)

	$c_{T,0}$	$c_{ef,0}$	$c_{ef,39}$
Cross correlation	0.3	0.5	0.01

The differences between estimations and measurements correspond to the velocity scatter of 5.9 m/s on 15 November found in section 5.1. The increasing accuracy of the estimations after 18 and 19 November might be explained by the presence of a stronger wind at 500 m height than at the ground (see Figure S1), which could cause a duct for the microbaroms below 500 m. Such a duct would reinforce a direct wave propagation between the stations. An explanation of the larger differences before the 18 November is that due to possible refractions in the lower atmosphere, instead of direct paths, uncertainties in the

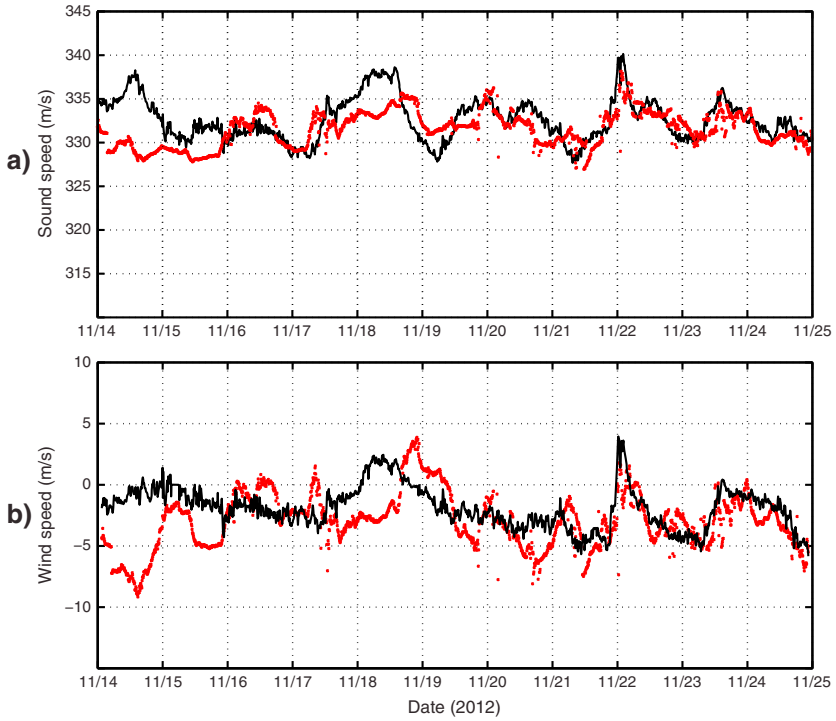

Figure 11. (a) Effective sound speed $c_{ef,0}$ (black line) provided by the ECMWF model in comparison with estimated effective sound speed $c_{est,0}$ (red dots). $c_{est,0}$ is found in a least squares estimation using the cross correlations of the stations RS206, RS307, and RS412. (b) Wind speed provided by ECMWF (black line) and estimated wind speed (red dots). The wind speed was determined by subtracting the adiabatic sound speed $c_{T,0}$ from the estimated effective sound speed $c_{est,0}$.

derived sound speed and wind arise. Refractions would result in estimations of the speed which are too low, since the delay time between the stations increases. This theory is supported by the ray tracing simulation (cf. section 5.1) in Figure 8, where we find refractions in the lower atmosphere near the array at the 15 November.

6. Conclusions

We successfully applied infrasonic interferometry to measured microbaroms. The delay time of the microbaroms between two stations is determined through cross correlating the recordings. This calculation for all 55 station pairs of the "Large Aperture Infrasound Array" (LAIA) gives the delay time of microbaroms up to a distance of 40.6 km; i.e., the infrasonic wave of the microbaroms is coherent up to this distance. The derived delay times are used to estimate the direction of arrival (DOA), which corresponds to the known microbarom sources in the north Atlantic Ocean. The strength of the 55 cross correlations were used to show that the coherence of the microbaroms along the DOA is higher than the coherence of those orthogonal to it. In a curve fitting of the coherence, we determined the sound speed scatter (±5.9 m/s) and the scatter of the incident angle (±1.7°), which follows *Mack and Flinn* [1971] and extends it to higher frequencies. The scattering of the sound speed lies within what can be assumed to be the range of sound speed variations caused by moderate winds. By comparing the wind speed to the strength of the cross correlation as a function of time, we can show that in our data set a strong meridional wind at the ground disturbs the delay time estimation. This can be explained by the higher noise levels due to the meridional wind in this specific case. Furthermore, uncertainties in the derived wind can arise due to possible refractions, instead of direct paths.

In a further comparison of the atmospheric state with a cross correlation as a function of time, we show that the infrasound propagation over the array is correlated to tropospheric temperature and wind. We could not find a correlation with the stratospheric conditions. Therefore, we conclude that we successfully applied infrasonic interferometry to microbaroms propagating in the troposphere between the stations.

Based on the cross correlations between three closest stations, we are able to estimate the effective sound speed and the wind speed as a function of time. Hence, infrasonic interferometry applied to tropospheric

propagating microbaroms is a promising approach for determining the effective sound speed and the wind speed at the ground. To probe the stratosphere with this technique, we need interstation or array distances of about 200 km, which is the average stratospheric shadow zone.

Acknowledgments
The described methods were applied to data, which can be obtained from the authors on request. We thank Matthew M. Haney for sharing his knowledge about the processing of microbaroms and cross correlations. P.S.M. Smets appreciates the support of the ARISE collaborative project, funded by the European Union (http://arise-project.eu). This research is funded by the Netherlands Organization for Scientific Research (NWO).

References

Antier, K., A. Le Pichon, S. Vergniolle, C. Zielinski, and M. Lardy (2007), Multiyear validation of the NRL-G2S wind fields using infrasound from Yasur, *J. Geophys. Res.*, *112*, D23110, doi:10.1029/2007JD008462.

Assink, J. D., R. Waxler, and D. Drob (2012), On the sensitivity of infrasonic traveltimes in the equatorial region to the atmospheric tides, *J. Geophys. Res.*, *117*, D01110, doi:10.1029/2011JD016107.

Assink, J. D., R. Waxler, W. G. Frazier, and J. Lonzaga (2013), The estimation of upper atmospheric wind model updates from infrasound data, *J. Geophys. Res. Atmos.*, *118*, 10,707–10,724, doi:10.1002/jgrd.50833.

Bensen, G. D., M. H. Ritzwoller, M. P. Barmin, A. L. Levshin, F. Lin, M. P. Moschetti, N. M. Shapiro, and Y. Yang (2007), Processing seismic ambient noise data to obtain reliable broad-band surface wave dispersion measurements, *Geophys. J. Int.*, *169*, 1239–1260.

Brekhovskikh, L. M., V. V. Goncharov, V. M. Kurtepov, and K. A. Naugolnykh (1973), The radiation of infrasound into the atmosphere by surface waves in the ocean, *Atmos. Oceanic Phys.*, *9*, 899–907.

Crescenti, G. H. (1997), A look back on two decades of Doppler sodar comparison studies, *Bull. Am. Meteorol. Soc.*, *78*, 651–673.

Donn, W. L., and B. Naini (1973), Sea wave origin of microbaroms and microseisms, *J. Geophys. Res.*, *78*, 4482–4488.

Drob, D. P., D. Broutman, M. A. Hedlin, N. W. Winslow, and R. G. Gibson (2013), A method for specifying atmospheric gravity wavefields for long-range infrasound propagation calculations, *J. Geophys. Res. Atmos.*, *118*, 3933–3943, doi:10.1029/2012JD018077.

Evers, L. G., and H. W. Haak (2001), Listening to sounds from an exploding meteor and oceanic waves, *Geophys. Res. Lett.*, *28*, 41–44.

Evers, L. G., and P. Siegmund (2009), Infrasonic signature of the 2009 major sudden stratospheric warming, *Geophys. Res. Lett.*, *36*, L23808, doi:10.1029/2009GL041323.

Fricke, J. T., N. E. Allouche, D. G. Simons, E. N. Ruigrok, K. Wapenaar, and L. G. Evers (2013), Infrasonic interferometry of stratospherically refracted microbaroms—A numerical study, *J. Acoust. Soc. Am.*, *134*, 2660–2668.

Godin, O. (2006), Recovering the acoustic Green's function from ambient noise cross correlation in an inhomogeneous moving medium, *Phys. Rev. Lett.*, *97*, 054301.

Godin, O. A., V. G. Irisov, and M. I. Charnotskii (2014), Passive acoustic measurements of wind velocity and sound speed in air, *J. Acoust. Soc. Am.*, *135*(2), EL68–EL74.

Gossard, E. E., and W. H. Hooke (1975), *Waves in the Atmosphere*, pp. 65–80, Elsevier Sci., Amsterdam.

Gutenberg, B. (1939), The velocity of sound waves and the temperature in the stratosphere in southern California, *Bull. Am. Meteorol. Soc.*, *20*, 192–201.

Haney, M. M. (2009), Infrasonic ambient noise interferometry from correlations of microbaroms, *Geophys. Res. Lett.*, *36*, L19808, doi:10.1029/2009GL040179.

Hasselmann, K. (1963), A statistical analysis of the generation of microseisms, *Rev. Geophys.*, *1*, 177–210.

Haubrich, R. A. (1968), Array design, *Bull. Seismol. Soc. Am.*, *58*, 977–991.

Holton, J. R. (2004), *An Introduction to Dynamic Meteorology*, pp. 183–227, Elsevier Acad. Press, Seattle, Wash.

Kedar, S., M. Longuet-Higgins, F. Webb, N. Graham, R. Clayton, and C. Jones (2008), The origin of deep ocean microseisms in the North Atlantic Ocean, *Proc. R. Soc. A*, *464*, 777–793.

Lalande, J. M., O. Sèbe, M. Landès, P. Blanc-Benon, R. S. Matoza, A. Le Pichon, and E. Blanc (2012), Infrasound data inversion for atmospheric sounding, *Geophys. J. Int.*, *190*, 687–701.

Le Pichon, A., E. Blanc, and D. Drob (2005), Probing high-altitude winds using infrasound, *J. Geophys. Res.*, *110*, D20104, doi:10.1029/2005JD006020.

Longuet-Higgins, M. S. (1950), A theory of the origin of microseisms, *Phil. Trans. R. Soc. A*, *243*, 1–35.

Mack, H., and E. A. Flinn (1971), Analysis of the spatial coherence of short-period acoustic-gravity waves in the atmosphere, *Geophys. J. Int.*, *26*, 255–269.

Marcillo, O., and J. B. Johnson (2010), Tracking near-surface atmospheric conditions using an infrasound network, *J. Acoust. Soc. Am.*, *128*, EL14–EL19.

Mentink, J. H., and L. G. Evers (2011), Frequency response and design parameters for differential microbarometers, *J. Acoust. Soc. Am.*, *130*, 33–41.

Posmentier, E. S. (1967), A theory of microbaroms, *Geophys. J. Int.*, *13*, 487–501.

Rind, D. H., and W. L. Donn (1978), Infrasound observations of variability during stratospheric warmings, *J. Atmos. Sci.*, *35*, 546–553.

Stopa, J. E., K. F. Cheung, M. A. Garcés, and N. Badger (2012), Atmospheric infrasound from nonlinear wave interactions during Hurricanes Felicia and Neki of 2009, *J. Geophys. Res.*, *117*, C12017, doi:10.1029/2012JC008257.

van Haarlem, M. P., et al. (2013), LOFAR: The LOw-Frequency ARray, *Astron. Astrophys.*, *556*(A2), 53.

Walker, K. T. (2012), Evaluating the opposing wave interaction hypothesis for the generation of microbaroms in the eastern North Pacific, *J. Geophys. Res.*, *117*, C12016, doi:10.1029/2012JC008409.

Wapenaar, K. (2006), Nonreciprocal Green's function retrieval by cross correlation, *J. Acoust. Soc. Am.*, *120*, EL7–EL13.

Waxler, R., and K. E. Gilbert (2006), The radiation of atmospheric microbaroms by ocean waves, *J. Acoust. Soc. Am.*, *119*, 2651.

Waxler, R., K. E. Gilbert, C. L. Talmadge, and C. Hetzer (2007), The effects of finite depth of the ocean on microbarom signals, paper presented at 8th International Conference on Theoretical and Computational Acoustics (ICTCA), Crete, Greece.